

Molecular Insights Into the Physics of Poly(amidoamine)-Dendrimer-Based Supercapacitors

Tarun Maity¹, Mounika Gosika^{1,2}, Tod A. Pascal³, and Prabal K. Maiti^{1,*}

¹*Center for Condensed Matter Theory, Dept. of Physics, Indian Institute of Science, Bangalore 560012, India*

²*Centro de Física de Materiales (CSIC, UPV/EHU) and Materials Physics Center MPC, Paseo Manuel de Lardizabal 5, San Sebastián 20018, Spain*

³*ATLAS Materials Physics Laboratory, Department of NanoEngineering and Chemical Engineering, University of California, San Diego, California 92023*

(Received 17 May 2022; revised 22 August 2022; accepted 10 October 2022; published 10 November 2022)

Increasing the energy density in electric double-layer capacitors (EDLCs), also known as supercapacitors, remains an active area of research. Specifically, there is a need to design and discover electrode and electrolyte materials with enhanced electrochemical storage capacity. Here, using fully atomistic molecular dynamics (MD) simulations, we investigate the performance of hyper-branched “poly(amidoamine) (PAMAM)” dendrimer as an electrolyte and an electrode coating material in a graphene-based supercapacitor. We investigate the performance of the capacitor using two different modeling approaches, namely the constant charge method (CCM) and the constant potential method (CPM). These simulations facilitated the direct calculation of the charge density, electrostatic potential, and field, and hence the differential capacitance. We found that the presence of the dendrimer in the electrodes and the electrolyte increased the capacitance by about 65.25% and 99.15%, respectively, compared with the bare graphene electrode-based aqueous EDLCs. Further analysis revealed that these increases were due to the enhanced electrostatic screening and reorganization of the double-layer structure of the dendrimer-based electrolyte.

DOI: 10.1103/PhysRevApplied.18.054031

I. INTRODUCTION

Improving the energy densities of electric double-layer capacitors (EDLCs), also known as supercapacitor-based energy devices, is of great practical interest [1–3], as these devices have higher power densities compared with conventional energy storage devices such as fuel cells, electrochemical batteries, and even dry/moist electrolytic capacitors. The improved energy density, in turn, would increase the commercial viability of EDLCs, thus spurring large-scale, mainstream adoption [4]. To this end, recent work has focused on engineering advanced electrode and electrolytes materials. Porous materials, with high specific surface areas and good electronic conductivity, have traditionally been used as electrode materials in these devices [5,6]. Room-temperature ionic liquids (RTILs) are typically chosen as the electrolyte, owing to their superior electrochemical properties, including high operating voltage windows and nonflammability, compared with aqueous and organic-based electrolytes [7]. Yet despite progress over the years in electrode and electrolyte optimization, further advances demand direct knowledge of the

interfacial structure and dynamics, and design principles for unique nanoscale physics therein.

In this work, we consider dendrimers: hyper-branched synthetic polymers as intriguing potential candidates as electrolytes in these devices [8]. Dendrimers have well-defined molecular structure, are flexible in size and shape, and are responsive to controllable stimuli such as pH [9–11]. They are also known to undergo structural deformations at interfaces [12,13] and their charge densities are comparable to those of ionic liquids [14]. Moreover, the pore size of a typical microporous electrode ranges from 0.5 to 5 nm, which matches well with the sizes of poly(amidoamine) (PAMAM) dendrimers, which vary from 0.6 nm for generation 0 (G0) to 6 nm for G10 [10,11,13,15]. Experiments and theory have shown that the capacitance in EDLCs is enhanced significantly when the pore size of the electrode material matches the size of the electrolyte ions [16,17].

Interfacial adsorption of dendrimers on electrodes dynamically exposes their charge groups to the electrolyte, which facilitates the formation of unique electric double-layer structures. This has been demonstrated by experiments by Guo *et al.* [18], who reported that hyper-branched polymers, such as dendrimers, exhibit very low losses in the dielectric response function, even at high operational

* maiti@iisc.ac.in; <http://www.physics.iisc.ernet.in/~maiti/>

frequencies (~ 1 MHz). Freire *et al.* [19] also showed that the presence of dendrimer can screen repulsive contacts between different counter ion molecules and favored ionic conductivity. These interesting properties of dendrimers make them potentially excellent candidates as electrolytes in EDLCs; however, a thorough microscopic examination of the interfacial behavior, and the resulting effect on electrochemical performance, have not yet been described.

Computer simulations employing molecular-dynamics-(MD)-based quantum mechanically derived accurate potentials (force fields) is a common tool for elucidating the microscopic nature of interfacial systems, and would be well suited for exploring the role of dendrimers in modulating the EDL structure and ultimately the performance of EDLCs. The key here is an accurate description of the interaction parameters, coarse-grained simulations revealed significant force-field dependence in the binding strength of dendrimers to graphene electrodes, as the system's pH [11] is varied [20]. To more clearly understand the nature of the interaction of the dendrimer-graphene composites requires us to go beyond coarse-grained force fields and perform fully atomistic simulations. Yet fully atomistic simulations of dendrimers at interfaces, where the dendrimer is being used as an electrolyte, are relatively rare to the best of our knowledge. In contrast, there have been several experimental [21,22] and simulation studies [23,24] that reported carbon-based electrode materials and studied the capacitance values with ionic liquids being the electrolytes [25]. For example, Trigueiro *et al.* [21] reported that the dendrimer-functionalized carbon nanotubes can improve the nanotube's performance as an electrode. Another study by Chandra *et al.* [26] reported that dendrimer-functionalized nanoparticles coating an electrode surface can enhance the surface area available to the electrolyte atoms, thereby achieving efficient charge transfer and low contact resistances. In another experimental work, Liu *et al.* [27] used a dendrimer-functionalized graphene-oxide sheet as a coating on the sulfur electrode of a Li-S battery and achieved long cycle life (up to 500 cycles). When considering common electrolytes in EDLCs, various computational studies on RTILs have been reported, including the work by Yeh and Berkowitz [28] which discussed the effect of periodic boundary conditions (PBCs) in EDLC simulations.

Recently, we used atomistic MD simulations to study the structural deformations [13] and the free-energy of the binding [29] of PAMAM dendrimers at a charge neutral graphene-water interface, as a function of the protonation state of the dendrimer. We found that the van der Waals interactions play a pivotal role in driving dendrimer adsorption. We also found that moderately charged (neutral pH) dendrimers achieve maximum surface wetting as compared with the nonprotonated (high-pH) and fully protonated (low-pH) dendrimers. We showed that lower generation dendrimers tended to deform and form flat,

disk-like architectures, with good surface accessibility, at the graphene-water interface [13]. These observations suggest that the lower generation PAMAM at neutral pH condition as an ideal choice for achieving maximum charge densities in PAMAM-based supercapacitors. Therefore, in this work, we considered a G2 PAMAM dendrimer at neutral pH, and elucidate the electrochemical performance in graphene-water-based EDLCs. Beyond accurate simulations of dendrimer based systems, we are also concerned with modeling biased nanoscale interfaces, as a means of probing electrochemical effects in EDLCs. Here, there are two main computation methods commonly employed for doing this: (1) the constant charge method (CCM) where the charges of the electrode atoms are fixed; and (2) the constant potential method (CPM) where a grand canonical statistical mechanical ensemble is defined by means of a fictitious bath that exchanges electrons with the electrodes to maintain a constant electrode potential (the number of electrons and chemical potential are conjugate pairs) [30,31]. The CPM approach is generally preferred as it enables simulations that are more directly comparable to experiments. However, it is somewhat restricted in its applicability due to significant additional computational demands. To this end, Wang *et al.* [30] compared both approaches for a LiClO_4 -acetonitrile-graphite EDLC and showed that both approaches lead to similar ion and solvent density profiles for voltages less than 2 V. Comparing the performance of both approaches for a more complicated electrode/electrolyte morphology is one of the aims of this study. Moreover, to address the computational challenges, Reed *et al.* [32] have developed an efficient approach for simulating cells within CPM [30] in the LAMMPS simulation engine, which we employ here.

This article is organized as follows. In Sec. II, we provide the model building and the simulation methodologies adopted in this work. In Sec. III, we present our results on the electrostatic potential, charge density profiles and the capacitance values, obtained from the CCM and the CPM approaches. Finally, in Sec. IV, we summarize our findings and conclude with the key insights from our study to provide future research directions.

II. MODEL AND SIMULATION DETAILS

In this work we focus on an aqueous supercapacitor simulation cell based on water/water+dendrimer electrolyte and graphene/dendrimer-coated graphene electrode (Table I). The initial structure of the PAMAM dendrimer was built using the Dendrimer Builder Toolkit (DBT) [15], whereas VMD [33] was used to build the graphene sheet. The aromatic carbon atoms of graphene were described using the AMBER FF10 force field (atom-type CA), as in our earlier works [34,35], which we showed captures the water-graphene interactions accurately. Intermolecular interactions involving dendrimer atoms were described by GAFF

TABLE I. Details of the electrode-electrolyte combinations studied. The structure of the dendrimer considered corresponds to a G2 PAMAM at neutral pH in all cases.

System	Positive Electrode (+15e)	Negative Electrode (-15e)	Electrolyte
BAREGP	Graphene	Graphene	H ₂ O
G2PEL	Graphene	Graphene	H ₂ O + G2 PAMAM + Cl ⁻ ions

GPDEN	Dendrimer-coated graphene	Graphene	H ₂ O
-------	---------------------------	----------	------------------

force field [36], the water molecules were modeled using the TIP3P [37,38] water model, and the Joung-Cheatham [39] parameters were used to model the Cl⁻ counter ions. Using the xLEaP module of AMBER 14 [40], the equilibrated electrolyte solution was placed between two graphene sheets with dimensions of 32.63 Å × 62.50 Å and separated by 150 Å.

We aim to understand how the presence of the dendrimer modifies the electrochemical charge storage and the capacitance values of the aqueous supercapacitor with a graphene electrode. Hence, we performed the simulations for a system with a two bare graphene electrode encapsulating a box of TIP3P waters, denoted BAREGP, as a control. To test the potential of using the dendrimer as an electrolyte and as an electrode, two additional systems, namely G2PEL and GPDEN, were considered. G2PEL comprised a G2 PAMAM dendrimer at neutral pH, immersed in a preequilibrated box of 10,118 TIP3P water molecules and placed between two graphene electrodes. We neutralize the system by adding 16 Cl⁻ counter ions (the charge of the G2 PAMAM at neutral pH is +16e) [10]. For the GPDEN system, we covalently grafted the G2 dendrimer onto the graphene electrode, using a “top binding and grafting to” approach, as detailed in our previous work [41]. Here, a dendrimer-grafted graphene was used as a positive electrode whereas a pristine graphene was used as a negative electrode. A total of 10,775 TIP3P water molecules were added between the two electrodes.

A. Constant Charge Method

We employed two different computational schemes for simulating applied bias in our systems. First, we used the PMEMD module of the AMBER14 [40] MD simulation suite to perform supercapacitor simulations with the CCM method. As mentioned previously, in the GPDEN case, the net charge of the dendrimer-coated graphene electrode was +15e, where charge of grafted dendrimer atom was adapted from Gosika *et al.* [41]. Thus, a charge of 0.01875e was distributed on each of the carbon atoms comprising the graphene electrode. In these studies, we

minimized spurious electrode-electrode electrostatic interactions by inserting a large 15-nm vacuum slab buffer in the z direction between the simulation cells, as shown in Fig. 1. For the BAREGP and G2PEL cases, we performed two sets of simulations, where the electrodes are (i) discharged (charge on every electrode atom is set to 0e), (ii) oppositely charged (charge on each electrode atom was set to 0.01875e, to be consistent with the GPDEN system). We initiated each simulation with 1000 steps of the steepest descent energy minimization, followed by a further 1000 steps of conjugate gradient minimization, to remove the initial bad contacts. We then gradually heated the system from 0 to 300 K using a Langevin thermostat with random friction collision frequency 1 ps⁻¹ in the constant temperature-constant volume (canonical or NVT) ensemble for 5 ns. During heating, we restrained the solute (electrode) atoms with a harmonic spring, with a force constant of 20 kcal mol⁻¹ Å⁻². Equilibrium MD simulations were then performed under the constant pressure-constant temperature (isothermal-isobaric or NPT) ensemble, with a weaker restraint (10 kcal mol⁻¹ Å⁻²) on graphene atoms (no restraint on dendrimer). The Langevin thermostat and Berendsen barostat were used to control the temperature at 300 K and pressure at 1 bar, respectively, with a collision frequency of 1 ps⁻¹ and pressure coupling constant of 0.5 ps. Finally, we performed 50-ns-long NVT production dynamics at 300 K, using a Langevin thermostat. The electrostatic interactions were evaluated using the particle mesh Ewald (PME) method [42] with a real space cutoff of 9 Å and a reciprocal space convergence tolerance of 5 × 10⁻⁴. The SHAKE algorithm [43] with a tolerance of 0.005 Å was used to constrain all bonds involving hydrogen atoms, as well as the H-O-H angle in water, to their equilibrium positions. This allowed us to use larger integration time steps of 2 fs. The trajectory from the final 10 ns of the MD simulations was used for statistical data analysis.

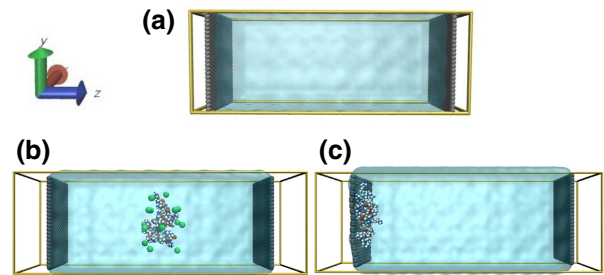


FIG. 1. Instantaneous snapshot of a simulation box representing (a) BAREGP, (b) G2PEL, and (c) GPDEN at 0 ns: positive electrode is on the left and negative is on the right. The dendrimer is shown in CPK. The graphene sheet is shown in gray. The protonated amines of the dendrimer are shown in blue and the Cl⁻ counter ions are colored green. The 15-nm vacuum slabs shown are not drawn to scale.

We obtained the electrostatic potential across the cell by solving the 2D Poisson's equation with xy symmetry. We set the field to be zero at both ends of the box (i.e., Neumann BCs) [44], and set the potential to be zero at the middle of the simulation cell. With these two BCs, one can formulate the expression for the potential as

$$\psi(z) = -\frac{1}{\epsilon_0} \int_{-D}^z dz' \int_{-D}^{z'} \rho(z'') dz'' - \psi(0), \quad (1)$$

where $\rho(z)$ is the charge density along the sheet's normal and $\psi(0)$ is the potential at the midpoint of the simulation box. The positive and negative electrodes are located at $-D$ and $+D$, respectively. Once the potential profiles were obtained, one can define the capacitance as [45]

$$C_s = \frac{|\sigma_s|}{\Delta \Delta \psi_{\text{cell}}}, \quad C_M = C_s \frac{A_0}{2M}. \quad (2)$$

Here,

$$\Delta \Delta \psi_{\text{cell}} = \Delta \psi_{\text{cell}}(\text{charged}) - \Delta \psi_{\text{cell}}(\text{discharged}) \quad (3)$$

and

$$\Delta \psi_{\text{cell}} = \psi(z = -D) - \psi(z = +D),$$

where σ_s , A_0 , and M are the charge density, area, and mass of the electrode, respectively, C_s is the area-specific capacitance with units of $\mu\text{F cm}^{-2}$, and C_M is the mass-specific capacitance with units of F g^{-1} [2].

B. Constant Potential Method

The CCM approach neglects the charge fluctuations on the electrode induced by local density fluctuations in the electrolyte solution. To explicitly take into account such physics, we also considered the CPM method which allows the charges on the electrode atoms to vary while maintaining a constant potential. We follow the implementation of the CPM method developed by Reed *et al.* [32] and later further improved by Gingrich and Wilson [46], based on earlier work of Siepmann and Sprik [47]. Here, the electric potential (ψ_i) on each electrode atom is constrained at each simulation step to be equal to a preset applied external potential V_{ext} , which is held constant. The charge on each electrode atom q_i (where i is the atom index of the electrode) is calculated self-consistently to satisfy the constraint condition: [32]

$$\psi_i = \frac{\partial U}{\partial q_i} = V_{\text{ext}}, \quad (4)$$

where U is the total coulomb energy of the system.

The starting structures for the CPM simulations were the equilibrated structures of the CCM simulations (discharge cases). All CPM simulations were performed using

the LAMMPS [30] MD package. The 20-ns NVT production simulations were performed using Nosé-Hoover thermostat at 300 K with a relaxation time of 100 fs, which was long enough to achieve the total charge equilibration of the electrodes. The cutoff used for the nonbonded interactions was 9 Å. The long-range electrostatic interactions were calculated by the particle-particle-particle-mesh Ewald summation method with a tolerance of 10^{-4} . Instead of using 2D periodic Ewald sums, we have used 3D periodic Ewald sums with shape corrections in this work to enhance the calculation speed, with a volume factor set to 3 [28]. The parameter of Gaussian charge distribution for the electrode atom was 19.79 nm^{-1} [32]. All the results reported here are the last 10 ns statistical averages.

The electrodes are maintained at a constant potential $\pm V_{\text{ext}}$ using the constant potential method (comp) module in LAMMPS [30]. To calculate the differential capacitance, we first calculated the averaged equilibrated charge density of the electrodes (which is a direct output from the CPM simulations) and applied the following equation:

$$C_{\text{diff}} = \frac{d\langle \sigma \rangle}{dV_{\text{ext}}}, \quad (5)$$

where $\langle \sigma \rangle$ is the equilibrated average surface charge density on the electrode. The mass-specific capacitance can be calculated from Eq. (2).

Note that one could also employ the constant pH method [48,49] to simulate dendrimer and dendrimer-coated graphene electrodes to investigate their behavior. However, the constant pH method is best suited to systems where the protonation state of the system is not very well known and has been used for some protein simulations. The situation is different in the case of dendrimer where titration experiments give the protonation state of dendrimer as a function of pH very accurately [50]. That is why dendrimer simulations in the literature are conducted taking into account the protonation states corresponding to a pH, as has been done in the present study. It is worth mentioning here that constant pH simulation for dendrimer [51] has also been shown to produce similar results to pH-dependent swelling using the same protocol used in our work. However, constant pH calculations require significant computational cost.

III. RESULTS AND DISCUSSIONS

A. CCM method

1. EDL structure

The structure of the electrode-electrolyte interface is an important property that gauges the performance of a supercapacitor. Hence, to understand the nature of the EDL structure and the distribution of the positive and the negatively charged entities of the system, we calculated their

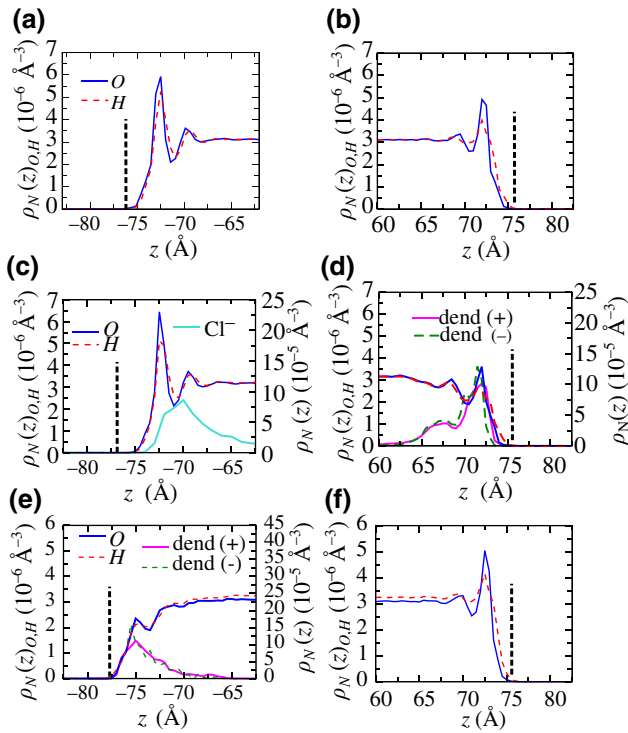


FIG. 2. Number density profiles for BAREGP at the (a) left and (b) right electrodes, obtained using the CCM method. (c)–(f) Profiles for G2PEL and GPDEN cases, at the left and right electrodes, respectively. The density profile of any given species is normalized by its total number in every case. We denote the positive and negative electrodes as L and R , denoting the left and right electrodes of the system. Number densities for hydrogen and oxygen scale with the left y axis whereas for dendrimer and Cl^- ions, it scales with the right y axis. Black dashed lines schematically represent the position of the graphene sheet.

number densities across the cell. In Fig. 2 we plot the normalized density profiles ($\rho_N(z)$) of the relevant charged species of the system, defined as

$$\rho_N(z)_{\text{species}} = \frac{1}{N_{\text{species}}} \frac{n(z, z + dz)}{L_x L_y dz}, \quad (6)$$

where N_{species} is the total number of a given species in the system, and $n(z, z + dz)$ is the number of the atoms of the species located between z and $z + dz$. Here L_x and L_y are the box dimensions in the x and y directions, respectively. By definition, $\int_{-D}^D \rho_N(z) L_x L_y dz = 1$.

In the case of BAREGP and GPDEN, there are no mobile anions or cations that would adsorb at the electrode's interface, thus electrostatic screening of the charged interface is only achieved by reorientation of the dipole of the water molecules. This fact, coupled with the nature of the electrode charge distribution, leads to notable changes in the interfacial water structure. For BAREGP, we find in Figs. 2(a) and 2(b) significant densification of the first layer waters compared with the bulk. Although

density fluctuations are commonly observed in fluids next to a hard wall (due to the reduction in dimensionality) [52], we find that the first shell water density and layer thickness on the left (positively charged) BAREGP electrode is greater than on the right (negatively charged), reflecting the directionality of the hydrogen bonding in water, which competes with the electrostatic screening effect that requires the water dipole point into the negative electrode (i.e., both hydrogens closer to the surface). The net effect is more disordered first layer at the negative electrode.

Turning our attention to the systems with the dendrimer, we find that the first layer water structure at the positively charged electrode of GPDEN [Fig. 2(e)] differs significantly from that of BAREGP and G2PEL [Fig. 2(a)]. This reflects the inhomogeneous charge distribution in GPDEN, where we have the dendrimer-coated graphene as the positively charged electrode [Fig. 2(e)]. In GPDEN, the water molecules can penetrate deeper into the electrode (i.e., dendrimer), so that the effective surface charge of the positively charged electrode is well compensated. By contrast, in the G2PEL system, the adsorption of the positively charged dendrimer at the right electrode (negatively charged) leads to best possible screening of the electrode's charge [Fig. 2(d)]. Similarly, the mobile Cl^- anions compensate for the positive charge of the left electrode [Fig. 2(c)]. Overall these microscopic EDL reorganization effects have a significant effect on the cell capacitance, as discussed in Sec. III B.

2. Potential profiles and capacitance values

The total charge densities of the systems at the left and the right electrodes are presented in Figs. 3(a) and 3(b), respectively, and encapsulate the results of the EDL structure in Sec. III A. For example, at the left electrode, the charge density for GPDEN is significantly less than for BAREGP [Fig. 3(a)], due to the better penetration of the water molecules into the electrode in the latter case. Similarly, we find that the charge density of G2PEL at the right electrode is less than that of BAREGP and GPDEN [Fig. 3(b)] due to the better screening of the electrode's charge by dendrimer adsorption [Fig. 2(d)]. Further, we obtained the electrostatic potential ($\psi(z)$) profiles across the cell using Eq. (1) as illustrated in Fig. 3(c) using the charge density data. We found a smaller potential difference across the electrodes for G2PEL and GPDEN compared with that observed in BAREGP (Table II). This results directly from the increased screening of the surface charge by the dendrimer, resulting in a reduced electric field and, hence, a smaller potential in the bulk region of the cell for G2PEL and GPDEN. Furthermore, in BAREGP and GPDEN, the large, finite slope in the potential profiles in the bulk region suggests a strong electric field in the middle of the simulation box, which is due to the heavily charged electrodes and the absence of

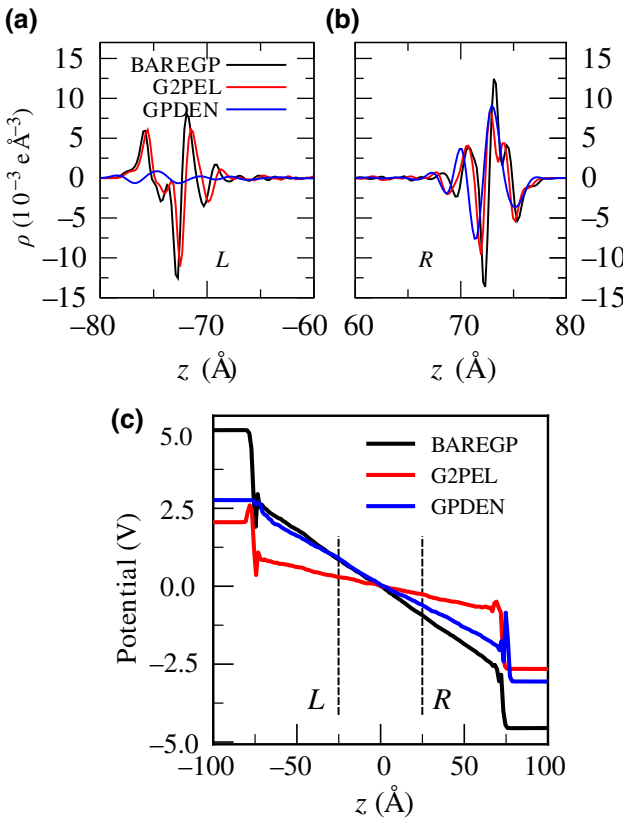


FIG. 3. (a),(b) In-plane averaged equilibrium charge density along the z direction. Subscripts L and R designate left and right, respectively. (c) Potential profile across the cell for BAREGP, G2PEL, and GPDEN cases for CCM. Presence of the dendrimer as an electrolyte and electrode reduces the potential difference across the simulation cell.

any potential screening effect due to free ionic salts, as evidenced by the reduced slope in the G2PEL system. Nevertheless, we do find a modulation of the potential drop at the electrode upon introduction of the dendrimer in the GPDEN system that is largely absent in BAREGP, which suggests better electrostatic screening compared with pristine graphene as an electrode.

To test this hypothesis and quantify the effect, we calculated the cell capacitance using Eq. (2) for all three systems and tabulated the values in Table II. This required us to perform both *charged* and *discharged* simulations

TABLE II. The potential difference across the cell and the capacitance values calculated using the CCM model.

System	$\Delta\psi_{\text{cell}}$ (dis) (V)	$\Delta\psi_{\text{cell}}$ (ch) (V)	C_s ($\mu\text{F}/\text{cm}^2$)	C_M (F/g)
BAREGP	0.12	9.53	1.18	6.58
GPDEN	0.12	5.86	1.95	11.03
G2PEL	0.04	4.75	2.35	13.14

TABLE III. Surface charge density of the virtual parallel plate capacitor. All the cases correspond to the *charged* simulation set.

System	σ_L ($10^{-4} \text{ e}\text{\AA}^{-2}$)	σ_R ($10^{-4} \text{ e}\text{\AA}^{-2}$)
BAREGP	1.98 ± 0.32	-2.08 ± 0.20
G2PEL	0.58 ± 0.28	-0.63 ± 0.19
GPDEN	1.87 ± 0.30	-1.54 ± 0.31

in order to compute the potential difference across the cell [Eq. (3)]. Although we performed these two sets of simulations for BAREGP and G2PEL, for GPDEN we performed only *charged* simulations, because we considered the discharged GPDEN case to be the same as the BAREGP system.

We found significantly higher capacitance in the two systems with the dendrimer, compared with BAREGP, with an increase of 65.25% and 99.15% for the dendrimer in electrode (GPDEN) and electrolyte (G2PEL) systems, respectively. To further understand the molecular origins of this effect, we divided our simulation cells into left ($z = -100$ Å to $z = -25$ Å) and right ($z = 25$ Å to $z = 100$ Å) subboxes. We consider a virtual parallel plate capacitor whose electrodes are now represented by these left and right regions, indicated by the two parallel line separators in Fig. 3.

The surface charge density σ_L is then calculated by integrating the charge density across each subbox, as follows:

$$\sigma_L(z) = \int_{-D}^z \rho(z) dz, \quad z \in [-55, -25], \quad (7)$$

$$\sigma_R(z) = \int_z^D \rho(z) dz, \quad z \in [25, 55]. \quad (8)$$

This allows us to reduce the fluctuations in a given bin during the simulation. The average values for σ are obtained using

$$\sigma_{L,R} = \langle \sigma_{L,R}(z) \rangle$$

and are presented in Table III.

For both the G2PEL and GPDEN cases, the net surface charge on the virtual parallel plate capacitor was found to be smaller than in BAREGP, again suggesting that the electrode's charge is better compensated for in the presence of the dendrimer. Here, in G2PEL, the solvated G2 PAMAM dendrimer behaves as a dielectric screening medium that decreases the strength of electric field, thus decreasing the potential and increasing the capacitance. Indeed, the dendrimer in GPDEN can be thought of as a porous electrode, where the availability of the charged groups accessible to the water molecules gives rise to the lowered potential difference.

B. Capacitance values: CPM method

Figures 4(a) and 4(b) show the accumulation of positive and negative charges density on the two electrodes in order to maintain ± 1 V, obtained using the CPM method. Equilibrium surface charge densities for all the voltages are included in Fig. 7 in Appendix.

Convergence was typically observed after approximately 10 ns of MD and we found that the presence of protonated G2 PAMAM dendrimer significantly affected the charge distributions compared with BAREGP. In Fig. 4(c) we depict the charge density σ of the positive electrode as a function of applied voltage for the BAREGP and G2PEL systems (the negative electrode acquired an opposite charge density). In both the cases, we found that the surface charge density of the electrode scaled linearly with applied potential, which implies a constant value of the differential capacitance over the potential range.

The values of the capacitance were then computed through a linear regression of the charge density data, shown in Fig. 4(c), with the results being $4.18 \mu\text{F cm}^{-2}$ and $5.84 \mu\text{F cm}^{-2}$ for BAREGP and G2PEL cases, respectively (Table IV). These capacitance and the surface charge

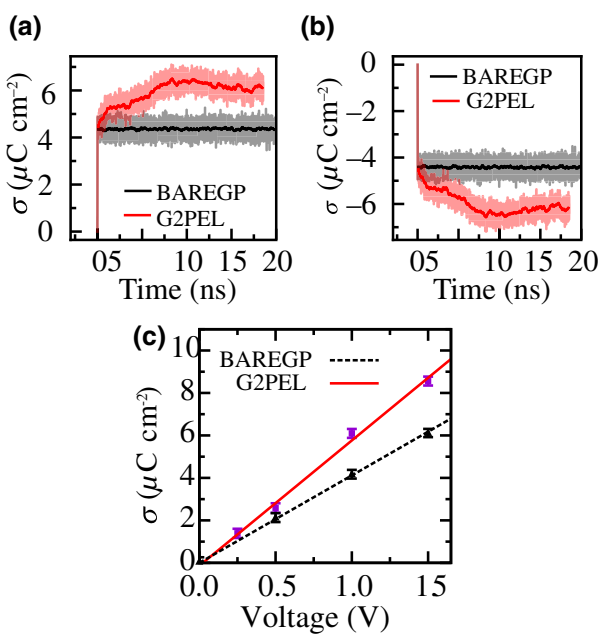


FIG. 4. Time evolution of the charge per unit area deposited on the (a) positive and (b) negative electrodes for BAREGP and G2PEL cases. The electrodes are maintained at fixed constant potentials ± 1 V, using the CPM algorithm. Presence of dendrimers accumulates more charge at electrodes to maintain 1 V. (c) Surface charge density on the positive electrode as a function of applied potential across the cell. The lines represent linear fits of the data. The corresponding slopes give the capacitance $5.84 \mu\text{F cm}^{-2}$ and $4.18 \mu\text{F cm}^{-2}$ for G2PEL and BAREGP cases, respectively.

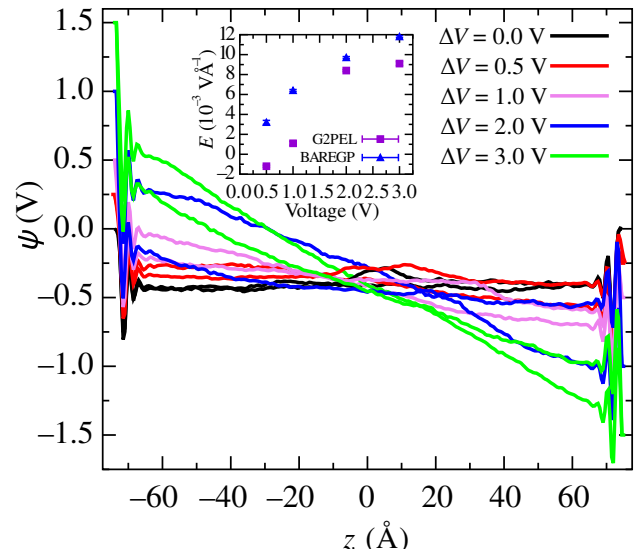


FIG. 5. Poisson potential (ψ) across the cell computed using Eq. (9) for different values of the applied voltage ΔV . Different colors represent different voltage. Solid and dashed lines represent BAREGP and G2PEL, respectively. The inset depicts the electric field inside the bulk region as a function of the applied potential difference in a cell.

density data are consistent with those reported in the literature for the BAREGP case [53]. Notably, we found a 39% increase in capacitance in G2PEL compared with BAREGP.

Further insights into the origin of the increased capacitance are obtained by computing the potential profile of the cell using the Poisson equation [44]:

$$\psi(z) = -\frac{1}{\epsilon_0} \int_{L_1}^z dz' \int_{L_1}^{z'} \rho(z'') dz'' + C_1(z - L_1) + V, \quad (9)$$

$$C_1 = \frac{1}{L_2 - L_1} \left[\Delta V + \frac{1}{\epsilon_0} \int_{L_1}^{L_2} dz' \int_{L_1}^{z'} \rho(z'') dz'' \right]. \quad (10)$$

Here we use Dirichlet BCs, $\psi(L_1 = -D) = V$, and $\psi(L_2 = D) = -V$. Figure 5 shows that the potential maintained a constant value within the electrode, oscillates in a region of 15 Å near the electrode interface, before exhibiting a linear profile in the bulk region. The oscillation of

TABLE IV. Differential capacitance values calculated using the CPM model.

System	$C_s (\mu\text{F cm}^{-2})$	$C_M (\text{F g}^{-1})$
BAREGP	4.18	23.35
G2PEL	5.84	32.62

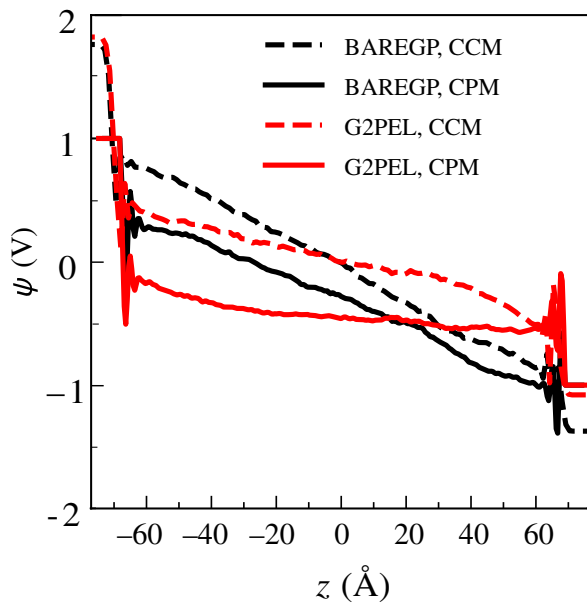


FIG. 6. Poisson's potential (ψ) profile for constant charge simulations, where a fixed charge is put on every atom of the electrodes corresponding to the average equilibrated charge on the electrode correspond to ± 1 V. Left: positive electrode; right: negative electrode.

the potential close to the electrode is due to water layering, resulting from intrinsic entropy-dominated forces at low voltage and stronger graphene-water interactions and electrostatic binding at larger potentials [54].

To understand how dendrimer affects the potential profile we calculated the electric field inside the bulk region (Table V). Here, we used the negative gradient of the potential in the bulk, from $-L'$ to L' , where $L' = D/2.5 \rightarrow D/3.3$. We found that as the voltage increases, so does the electric field in the bulk region (Table V). Figure 5 shows that for G2PEL, the strength of the electric field was reduced in the bulk region, as compared with BAREGP, due to electrostatic screening of the dendrimer at all voltages. In other words, in order to maintain the required voltage, the G2PEL system has to store more charge than BAREGP.

TABLE V. Electric field in the bulk region of electrolyte of BAREGP and G2PEL at different voltages.

ΔV (V)	E (10^{-3} V Å $^{-1}$) in BAREGP	E (10^{-3} V Å $^{-1}$) in G2PEL
0.5	3.2 ± 0.2	1.2 ± 0.1
1.0	6.4 ± 0.1	1.1 ± 0.2
2.0	9.7 ± 0.1	8.4 ± 0.1
3.0	11.8 ± 0.1	9.1 ± 0.2

TABLE VI. Comparison of capacitance computed using CPM and CCM.

System	$\Delta\psi$ (V)		C_s ($\mu\text{F cm}^{-2}$)	
	CPM	CCM	CPM	CCM
BAREGP	2.0	3.14	2.08	1.32
G2PEL	2.0	2.85	2.59	1.89

C. Comparison between CCM and CPM approaches

To compare the CCM and CPM method, we performed additional simulations using the CCM method, where total charge on each electrode was taken as the average equilibrated charge in the CPM method at ± 1 V, distributed evenly on each carbon atom of the graphene sheet.

Figure 6 reports the Poisson's potential across the simulation cell for both methods. The solid curves are the results obtained from CPM method using Dirichlet BCs (9) and dashed curves are the potential profile corresponding to the CCM method using Newman's BCs (1). The corresponding data are listed in Table VI. Our results using the CPM method compare well to reported values in the literature [53]. We found that although the CCM method predicted consistent capacitive enhancements in the G2PEL system compared with BAREGP, it generally overestimated the value of the potential in both cases. Thus, we conclude that although the CCM method may be adequate to obtain qualitative insights into the electrochemical behavior of these systems, more detailed, quantitative results will require the CPM method.

IV. CONCLUSIONS AND FUTURE OUTLOOK

To summarize, we have used extensive MD simulations to show that the presence of a protonated G2 PAMAM dendrimer, in aqueous solutions or grafted on the electrode, enhances the capacitance and reduces the potential across the cell significantly compared with pristine graphene electrodes. The EDL structure and overall cell performance was shown to be a dramatic function of the dendrimer morphology (free or grafted) and chemistry (charged or neutral), suggesting two different ways to utilize dendrimers with the aim of improving the capacitances of the graphene-based aqueous supercapacitors. Further, these results advance our understanding of the role of macromolecules in modifying the properties of electrochemical systems and suggest important avenues for predictive design for improved efficiencies.

ACKNOWLEDGMENTS

TM thanks MoE, India, for financial support in the form of scholarship. We also acknowledge computational support through TUE-CMS, IISc funded by DST, India. We

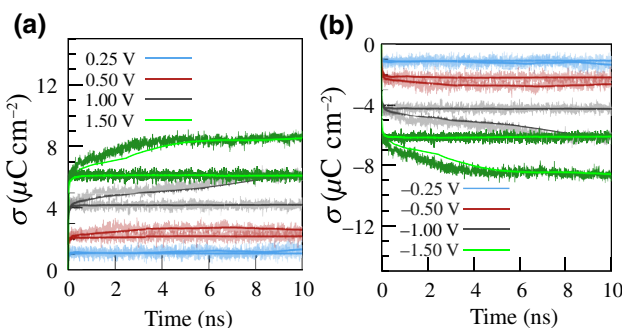


FIG. 7. (a),(b) Equilibrium charge densities in the positive electrode and negative electrode, respectively. Solid and dashed lines represent G2PEL and BAREGP, respectively. Different colors represent different voltages. For all the voltages, the G2PEL case required more charge on the electrode to maintain a fixed voltage compared with BAREGP.

also thank Supercomputer Education and Research Center (SERC), IISc, for providing supercomputer time at CRAY, SAHASRAT machine. PKM acknowledges funding through SERB, IRHPA (No.IPA/2020/000034).

APPENDIX A: CHARGE DENSITY PROFILES AS A FUNCTION OF THE APPLIED VOLTAGE

Figures 7(a) and 7(b) show the accumulation of charge densities on the positive and negative electrode respectively to maintain the external voltage.

- [1] J. Vatamanu and D. Bedrov, Capacitive energy storage: current and future challenges, *J. Phys. Chem. Lett.* **6**, 3594 (2015).
- [2] J. Vatamanu, M. Vatamanu, and D. Bedrov, Non-faradaic energy storage by room temperature ionic liquids in nanoporous electrodes, *ACS Nano* **9**, 5999 (2015).
- [3] J. Vatamanu, L. Cao, O. Borodin, D. Bedrov, and G. D. Smith, On the influence of surface topography on the electric double layer structure and differential capacitance of graphite/ionic liquid interfaces, *J. Phys. Chem. Lett.* **2**, 2267 (2011).
- [4] B. E. Conway, *Electrochemical Supercapacitors: Scientific Fundamentals and Technological Applications* (Springer Science & Business Media, New York, 2013).
- [5] P. Barpanda, G. Fanchini, and G. G. Amatucci, Structure, surface morphology and electrochemical properties of brominated activated carbons, *Carbon* **49**, 2538 (2011).
- [6] M. Zhi, C. Xiang, J. Li, M. Li, and N. Wu, Nanostructured carbon–metal oxide composite electrodes for supercapacitors: a review, *Nanoscale* **5**, 72 (2013).
- [7] P. Simon and Y. Gogotsi, Materials for electrochemical capacitors, *Nanoscience and technology: a collection of reviews from Nature journals*, 3202010.
- [8] J. Li, L. Pielher, D. Qin, J. Baker, D. Tomalia, and D. Meier, Visualization and characterization of poly (amidoamine)

dendrimers by atomic force microscopy, *Langmuir* **16**, 5613 (2000).

- [9] R. Esfand and D. A. Tomalia, Poly (amidoamine)(pamam) dendrimers: from biomimicry to drug delivery and biomedical applications, *Drug Discov. Today* **6**, 427 (2001).
- [10] P. K. Maiti, T. Çağın, G. Wang, and W. A. Goddard, Structure of pamam dendrimers: Generations 1 through 11, *Macromolecules* **37**, 6236 (2004).
- [11] P. K. Maiti, T. Çağın, S.-T. Lin, and W. A. Goddard, Effect of solvent and ph on the structure of pamam dendrimers, *Macromolecules* **38**, 979 (2005).
- [12] T. Lin, I.-W. Chen, F. Liu, C. Yang, H. Bi, F. Xu, and F. Huang, Nitrogen-doped mesoporous carbon of extraordinary capacitance for electrochemical energy storage, *Science* **350**, 1508 (2015).
- [13] M. Gosika and P. K. Maiti, ph and generation dependent morphologies of pamam dendrimers on a graphene substrate, *Soft Matter* **14**, 1925 (2018).
- [14] T. C. Lin, *Poly (amido amine) Dendrimers in Supercapacitors*, Tech. Rep. (institution Los Alamos National Lab.(LANL), Los Alamos, NM (United States), 2013).
- [15] V. Maingi, V. Jain, P. V. Bharatam, and P. K. Maiti, Dendrimer building toolkit: Model building and characterization of various dendrimer architectures, *J. Comput. Chem.* **33**, 1997 (2012).
- [16] C. Largeot, C. Portet, J. Chmiola, P.-L. Taberna, Y. Gogotsi, and P. Simon, Relation between the ion size and pore size for an electric double-layer capacitor, *J. Am. Chem. Soc.* **130**, 2730 (2008).
- [17] C. Merlet, B. Rotenberg, P. A. Madden, P.-L. Taberna, P. Simon, Y. Gogotsi, and M. Salanne, On the molecular origin of supercapacitance in nanoporous carbon electrodes, *Nat. Mater.* **11**, 306 (2012).
- [18] M. Guo, X. Yan, Y. Kwon, T. Hayakawa, M.-a. Kakimoto, and T. Goodson, High frequency dielectric response in a branched phthalocyanine, *J. Am. Chem. Soc.* **128**, 14820 (2006).
- [19] J. J. Freire, A. Ahmadi, and C. McBride, Molecular dynamics simulations of the protonated g4 pamam dendrimer in an ionic liquid system, *J. Phys. Chem. B* **117**, 15157 (2013).
- [20] K. Maerzke, N. Henson, P. Welch, and C. Welch, in *ABSTRACTS OF PAPERS OF THE AMERICAN CHEMICAL SOCIETY*, Vol. 249 (AMER CHEMICAL SOC 1155 16TH ST, NW, WASHINGTON, DC 20036 USA, 2015).
- [21] J. P. C. Trigueiro, R. C. Figueiredo, J. Rojo, R. M. Viana, M. C. Schnitzler, and G. G. Silva, Carbon nanotube/dendrimer hybrids as electrodes for supercapacitors, *J. Solid State Electrochem.* **20**, 1991 (2016).
- [22] T. Rath and P. P. Kundu, Reduced graphene oxide paper based nanocomposite materials for flexible supercapacitors, *RSC Adv.* **5**, 26666 (2015).
- [23] Y. Shim, Y. Jung, and H. J. Kim, Graphene-based supercapacitors: A computer simulation study, *J. Phys. Chem. C* **115**, 23574 (2011).
- [24] M. Salanne, B. Rotenberg, K. Naoi, K. Kaneko, P.-L. Taberna, C. P. Grey, B. Dunn, and P. Simon, Efficient storage mechanisms for building better supercapacitors, *Nat. Energy* **1**, 1 (2016).

- [25] X. Mao, P. Brown, C. Červinka, G. Hazell, H. Li, Y. Ren, D. Chen, R. Atkin, J. Eastoe, and I. Grillo, *et al.*, Self-assembled nanostructures in ionic liquids facilitate charge storage at electrified interfaces, *Nat. Mater.* **18**, 1350 (2019).
- [26] S. Chandra, M. D. Patel, H. Lang, and D. Bahadur, Dendrimer-functionalized magnetic nanoparticles: a new electrode material for electrochemical energy storage devices, *J. Power Sources* **280**, 217 (2015).
- [27] W. Liu, J. Jiang, K. R. Yang, Y. Mi, P. Kumaravadivel, Y. Zhong, Q. Fan, Z. Weng, Z. Wu, and J. J. Cha, *et al.*, Ultra-thin dendrimer-graphene oxide composite film for stable cycling lithium-sulfur batteries, *Proc. Nat. Acad. Sci.* **114**, 3578 (2017).
- [28] I.-C. Yeh and M. L. Berkowitz, Ewald summation for systems with slab geometry, *J. Chem. Phys.* **111**, 3155 (1999).
- [29] M. Gosika, S. Sen, A. Kundagrami, and P. K. Maiti, Understanding the thermodynamics of the binding of pamam dendrimers to graphene: A combined analytical and simulation study, *Langmuir* **35**, 9219 (2019).
- [30] Z. Wang, Y. Yang, D. L. Olmsted, M. Asta, and B. B. Laird, Evaluation of the constant potential method in simulating electric double-layer capacitors, *J. Chem. Phys.* **141**, 184102 (2014).
- [31] C. Merlet, B. Rotenberg, P. A. Madden, and M. Salanne, Computer simulations of ionic liquids at electrochemical interfaces, *Phys. Chem. Chem. Phys.* **15**, 15781 (2013).
- [32] S. K. Reed, O. J. Lanning, and P. A. Madden, Electrochemical interface between an ionic liquid and a model metallic electrode, *J. Chem. Phys.* **126**, 084704 (2007).
- [33] W. Humphrey, A. Dalke, and K. Schulten, Vmd: visual molecular dynamics, *J. Mol. Graph.* **14**, 33 (1996).
- [34] H. Kumar, C. Dasgupta, and P. K. Maiti, Phase transition in monolayer water confined in janus nanopore, *Langmuir* **34**, 12199 (2018).
- [35] J. Majumdar, M. Moid, C. Dasgupta, and P. K. Maiti, Dielectric profile and electromelting of a monolayer of water confined in graphene slit pore, *J. Phys. Chem. B* **125**, 6670 (2021).
- [36] J. Wang, R. M. Wolf, J. W. Caldwell, P. A. Kollman, and D. A. Case, Development and testing of a general amber force field, *J. Comput. Chem.* **25**, 1157 (2004).
- [37] W. L. Jorgensen, J. Chandrasekhar, J. D. Madura, R. W. Impey, and M. L. Klein, Comparison of simple potential functions for simulating liquid water, *J. Chem. Phys.* **79**, 926 (1983).
- [38] D. J. Price and C. L. Brooks III, A modified tip3p water potential for simulation with ewald summation, *J. Chem. Phys.* **121**, 10096 (2004).
- [39] I. S. Joung and T. E. Cheatham III, Determination of alkali and halide monovalent ion parameters for use in explicitly solvated biomolecular simulations, *J. Phys. Chem. B* **112**, 9020 (2008).
- [40] D. A. Case, V. Babin, J. Berryman, R. Betz, Q. Cai, D. Cerutti, T. Cheatham Iii, T. Darden, R. Duke, and H. Gohlke, *et al.*, *Amber 14* (University of California, San Francisco, 2014).
- [41] M. Gosika, V. Velachi, M. N. D. Cordeiro, and P. K. Maiti, Covalent functionalization of graphene with pamam dendrimer and its implications on graphene's dispersion and cytotoxicity, *ACS Appl. Polym. Mater.* **2**, 3587 (2020).
- [42] T. Darden, D. York, and L. Pedersen, Particle mesh ewald: An n log (n) method for ewald sums in large systems, *J. Chem. Phys.* **98**, 10089 (1993).
- [43] J.-P. Ryckaert, G. Ciccotti, and H. J. Berendsen, Numerical integration of the cartesian equations of motion of a system with constraints: molecular dynamics of n-alkanes, *J. Comput. Phys.* **23**, 327 (1977).
- [44] D. Boda and D. Gillespie, Calculating the electrostatic potential profiles of double layers from simulation ion density profiles, *Hung. J. Ind. Chem.* **41**, 123 (2013).
- [45] S.-W. Park, A. D. DeYoung, N. R. Dhumal, Y. Shim, H. J. Kim, and Y. Jung, Computer simulation study of graphene oxide supercapacitors: charge screening mechanism, *J. Phys. Chem. Lett.* **7**, 1180 (2016).
- [46] T. R. Gingrich and M. Wilson, On the ewald summation of Gaussian charges for the simulation of metallic surfaces, *Chem. Phys. Lett.* **500**, 178 (2010).
- [47] J. I. Siepmann and M. Sprik, Influence of surface topology and electrostatic potential on water/electrode systems, *J. Chem. Phys.* **102**, 511 (1998).
- [48] A. M. Baptista, V. H. Teixeira, and C. M. Soares, Constant-p h molecular dynamics using stochastic titration, *J. Chem. Phys.* **117**, 4184 (2002).
- [49] M. Machuqueiro and A. M. Baptista, Constant-ph molecular dynamics with ionic strength effects: Protonation-conformation coupling in decalysine, *J. Phys. Chem. B* **110**, 2927 (2006).
- [50] R. C. van Duijvenbode, M. Borkovec, and G. J. Koper, Acid-base properties of poly (propylene imine) dendrimers, *Polymer* **39**, 2657 (1998).
- [51] P. B. Reis, D. Vila-Vicosa, S. R. Campos, A. M. Baptista, and M. Machuqueiro, Role of counterions in constant-ph molecular dynamics simulations of pamam dendrimers, *ACS Omega* **3**, 2001 (2018).
- [52] M. P. Allen and D. J. Tildesley, *Computer Simulation of Liquids* (Oxford university press, New York, 2017).
- [53] G. Jeanmairet, B. Rotenberg, D. Borgis, and M. Salanne, Study of a water-graphene capacitor with molecular density functional theory, *J. Chem. Phys.* **151**, 124111 (2019).
- [54] T. A. Pascal and W. A. Goddard III, Entropic stabilization of water at graphitic interfaces, *J. Phys. Chem. Lett.* **12**, 9162 (2021).